



Article

Protection Coordination Strategy for the Distributed Electric Aircraft Propulsion Systems

Anil Kumar Reddy Siddavatam¹, Kaushik Rajashekara^{1,*} , Hao Huang¹ and Fred Wang²

¹ Department of Electrical and Computer Engineering, University of Houston, Houston, TX 77204, USA; asiddava@cougarnet.uh.edu (A.K.R.S.); hhao4@central.uh.edu (H.H.)

² Department of Electrical Engineering and Computer Science, University of Tennessee, Knoxville, TN 37996, USA; fred.wang@utk.edu

* Correspondence: ksraja@central.uh.edu

Abstract: The current trend in distributed electric aircraft propulsion systems is to utilize the DC bus system at higher voltage levels than conventional aircraft systems. With Boeing and Airbus utilizing the ± 270 V bipolar DC bus system, the research on high-voltage systems is increasing gradually, with voltage levels ranging from 1 to 10 kV systems or ± 0.5 to ± 5 kV DC bus systems. These voltage levels present considerable challenges to the distributed electric aircraft propulsion systems. In addition to partial discharge effects, there are other challenges, particularly the challenge associated with effectively limiting short-circuit fault currents due to the low cable impedance of the distribution system. The cable impedance is a significant factor that determines the fault current during fault conditions. Due to the low impedance, there is a sharp increase in fault current, necessitating an enhanced protection strategy, which ensures that the system is adequately protected. This paper introduces a coordinated protection strategy specifically designed for distributed electric aircraft propulsion systems to mitigate or prevent short-circuit faults. The proposed algorithm utilizes an I^2t -based strategy and the current-limiting-based strategy to protect the system from short-circuit faults and overload conditions. Redundant backup protection is also included in the algorithm in case the circuit breaker fails to operate.

Keywords: electric aircraft; distributed electric aircraft propulsion (DEAP); solid state circuit breakers; I^2t protection; current limiting; protection coordination



Citation: Siddavatam, A.K.R.; Rajashekara, K.; Huang, H.; Wang, F. Protection Coordination Strategy for the Distributed Electric Aircraft Propulsion Systems. *World Electr. Veh. J.* **2024**, *15*, 187. <https://doi.org/10.3390/wevj15050187>

Academic Editor: Joeri Van Mierlo

Received: 15 February 2024

Revised: 22 March 2024

Accepted: 24 April 2024

Published: 28 April 2024



Copyright: © 2024 by the authors. Licensee MDPI, Basel, Switzerland. This article is an open access article distributed under the terms and conditions of the Creative Commons Attribution (CC BY) license (<https://creativecommons.org/licenses/by/4.0/>).

1. Introduction

Globally, the aerospace industry produces about 3% of the total carbon dioxide emissions. Commercial aircraft are mostly responsible for this. In order to reduce these emissions, the aerospace industry has made significant advancements in electrifying aircraft and has already commercialized more electric aircraft (MEA), such as the Boeing 787, Airbus 380, and Airbus 350 [1]. Pneumatic and hydraulic systems in these aircraft are replaced with the electrical systems. These aircraft use high levels of electric power for the onboard systems, such as environmental control systems (ECS), flight control systems, emergency systems, landing gear systems, in-flight entertainment systems, health monitoring systems, anti-ice systems, etc. The technology and challenges of the more electric aircraft systems are outlined in [2,3]. Although the MEA has improved performance and provided other advantages, such as increased fuel efficiency, reduced emissions, and reduced weight, the focus of these systems is only on the non-propulsive systems. To replace the traditional engines with the propulsion motors, the electrical power required would be of the order of several megawatts. With the current battery technology, it is not feasible to propel these aircraft (Airbus A 380 and Boeing 737) with battery power alone. Using battery power, pure electric aircraft can only be designed for shorter distances with less than 15 passengers. For example, the aircraft designed by an Eviation company named “Alice” made its

first flight in September 2022, which is designed to carry nine passengers with a range of 250 nautical miles [4]. For long distance travel, hybrid electric aircraft would be best to reduce emissions [2]. For large electric aircraft with more than 100 passengers, distributed electric aircraft propulsion (DEAP) architectures offer several advantages, such as higher efficiency and independent control of propulsion motors [5].

The first electric aircraft that was based on the distributed electric aircraft propulsion architecture was the NASA Maxwell X-57 with 12 small electric propulsion motors placed at the edge of the wings and two large electric propulsion motors (cruise motors) at the wingtips [6]. It is developed by modifying the Tecnam P2006T aircraft by solely powering the electric propulsion motor drives using the battery packs. With the 12 small propulsion motors situated along the wing, the wing can produce more lift even at low speeds due to the increased airflow caused by the propulsion motors. Furthermore, the independent control of each electric propulsion motor allows the aircraft to adapt to flying conditions such as wind gusts by changing the over-wing airflow pattern. Another example of a distributed electric aircraft propulsion system is NASA N3-X [7] with 16 propulsion motors driven by four turbo electric generators connected to two turbines. Different architecture configurations for the distributed electric aircraft propulsion systems are proposed in the literature to make the NASA N3-X radial architecture fault tolerant without losing many propulsion motors for single-point failures [8–10]. This ultimately led to the addition of redundant cables and circuit breakers to the systems leading to increased overall weights [11]. NASA N3-X initially had fourteen propulsion motors in its architecture, but due to the asymmetrical thrust generated in case of a fault (generator out of service or bus bar fault) in the system, this configuration was later changed to sixteen propulsion motors, which are equally distributed on both wings [10]. To address these issues, different fault-tolerant architectures are proposed in the literature, namely, inner bus tie (IBT) [7], three-bus multi-feeder (TBM) [12], cross-redundant multi-feeder (CRM) [7], four-bus inner bus tie (FBT) [13], fault-tolerant architecture 1 and 2 (FTA 1 and 2) [14], and H type [15] architectures. These architectures isolate only one out of sixteen propulsion motors for a single point failure in the system. However, none of the architectures mentioned has discussed the protection coordination strategies, which play a crucial role in the architectures involving multiple electric propulsion motors and power sources.

The NASA N3-X architecture uses a DC distribution system in which the electrical power is generated by the turboelectric generators and then converted to DC power using AC-DC converter. The DC power is now used to feed the electric propulsion motors with the help of a DC-AC converter. Each propulsion motor is operated at 1 MW of power, and a total of 16 MW power is required to drive these propulsion motors. To feed such a large amount of power, operating at the voltage level of ± 270 V used in Boeing 787 is practically not feasible. This lower voltage level results in increased power losses, thus increasing the heat produced and resulting in an increase in the size of cables, converters, etc. In a 2 MW system, the optimum voltage of 4 kV is desirable to efficiently transmit the power in the cables, and for a 20 MW system, the optimum voltage required is about 10 kV. In such high-voltage systems (10 kV) with very low cable inductances, the short-circuit fault in the system causes the current to rise sharply in a short time, which could lead to the damage of several electrical components, including cables. Traditional over-current protection strategies that are designed to protect the system from the over-current faults can trip the circuit breakers and isolate the fault. However, these strategies may also trip the circuit breaker during transients that last for a very short period. Therefore, this type of system requires more advanced protection methods, such as current squared through time (I^2t) and current-limiting strategies. These strategies are intended to quickly detect overcurrent faults and provide more effective protection without falsely triggering the circuit breakers. Adding the current-limiting strategies to the circuit breakers in the system helps in reducing the fault current magnitude by introducing the impedance of the circuit breaker into the system. This gives extra reaction time for the circuit breakers that use the

I^2t algorithm leading to enhanced protection of the system. These strategies also help in protecting the system from overloading conditions.

The main body of this paper is organized into four sections. Section 2 provides an overview of the radial baseline architecture. Section 3 discusses the proposed protection co-ordination strategy, Section 4 discusses the I^2t curves of the components in the system, and Section 5 presents simulation results for the proposed protection coordination algorithm. The paper is concluded by summarizing the proposed strategy and results.

2. Radial Baseline Architecture

The typical radial baseline architecture is shown in Figure 1. There are four independent distributed electric propulsion channels, each of which includes a (i) generator, (ii) AC-DC converter, (iii) cables, (iv) eight distribution network circuit breakers (e.g., CBx; $x = 3, 4, 5, 6, 7, 8$), (v) four transmission network circuit breakers (e.g., CB1, CB2, CB11, and CB12), (vi) four DC-AC converters, (vii) four propulsion motors, (viii) battery, (ix) one DC-DC converter, and (x) a set of non-propulsion loads. The turbine-driven generators are connected to the AC-DC converters to convert AC power to DC power. The converted DC power is then fed to the DC-AC converter to drive the four propulsion motors using the transmission and distribution network cables. The battery energy storage system is designed to drive two propulsion motors in each channel for safe landing of the aircraft under emergency conditions. In addition, it can also be used to provide peak power during faults in the system.

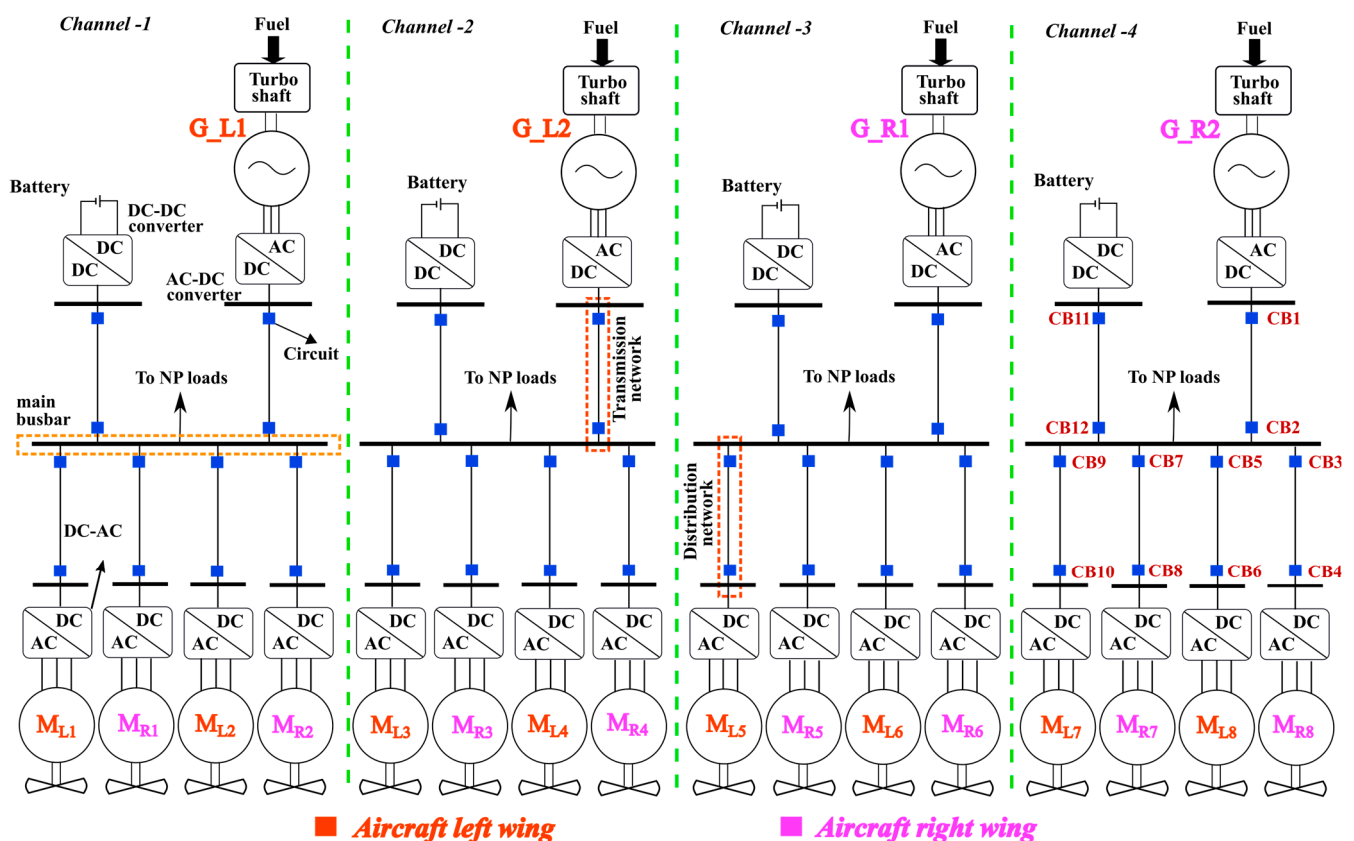


Figure 1. Radial baseline architecture.

For a short-circuit fault between circuit breakers CB3 and CB4 (shown in Figure 1), the motor M_{R8} has to be isolated by tripping the circuit breakers CB3 and CB4. To achieve this, the current sensors in the circuit breakers are used. The current flowing through the circuit breaker is considered positive if the current direction is toward the motors and considered negative when the current flows in the opposite direction as shown in Figure 2. The current

sensors in the circuit breakers CB3, CB5, CB7, and CB9 are placed in such a manner that the current flowing through them is positive, and current through the circuit breakers CB4, CB6, CB8, and CB10 is negative during normal operation. In the event of a short-circuit fault between circuit breaker CB3 and CB4, the fault current is positive through the circuit breaker CB3 and negative through the circuit breaker CB4, as the capacitor at the input of the DC-AC converter is short-circuited through the low impedance path of the cable as shown in Figure 2.

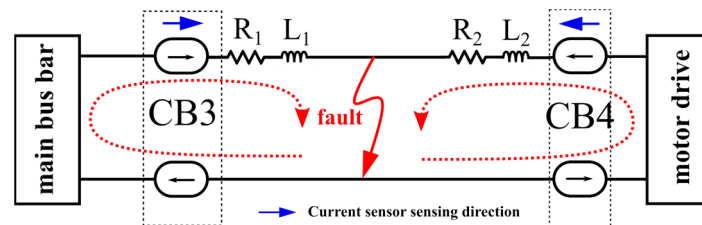


Figure 2. Fault location in the distribution network (cable connecting motor M_{R8}).

The circuit breakers CB_x ($x = 1$ to 12) are unidirectional breakers, which protect the system only if the fault current through them matches the arrow direction (blue) shown in Figure 2. When a fault occurs in the system, the capacitors at the input of all the DC/AC converters see a very low impedance path, leading to current flow in a reverse direction and contributing to the fault current. The downstream circuit breakers (CB4, 6, 8 and 10) are operated in the current limit mode to avoid this. If the upstream circuit breakers (CB3, 5, 7, and 9) are operated in current limit mode, then the fault current through the faulty distribution network, which is very high in magnitude when compared with the healthy distribution network currents (reverse current), leads to an increase in on-state resistance of the SSCB. To reduce the heat produced due to the increased on-state resistance, enhanced cooling solutions should be used to prevent thermal runaway.

For a fault in the distribution network and transmission network, the responsible circuit breakers that must trip and the protection strategy are shown in Table 1.

Table 1. Fault location vs. protection methods for the responsible circuit breakers.

Fault Location	Responsible Circuit Breakers	Protection Methods	Backup Protection
Between CB1 and CB2	CB1 and CB2	CB1— I^2t protection CB2—current limit mode	Rectifier has to protect if CB1 fails
Between CB3 and CB4	CB3 and CB4	CB3— I^2t protection CB4—current limit mode	CB1
Between CB5 and CB6	CB5 and CB6	CB5— I^2t protection CB6—current limit mode	CB1
Between CB7 and CB8	CB7 and CB8	CB7— I^2t protection CB8—current limit mode	CB1
Between CB9 and CB10	CB9 and CB10	CB9— I^2t protection CB10—current limit mode	CB1

3. Proposed Protection Coordination Algorithm

The proposed protection coordination algorithm for the radial baseline architecture is shown in Figure 3. The currents through the circuit breakers in the system are measured and then compared with the respective preset values. Under healthy operation, the nominal current flowing through the distribution network is around 100 A, and when the fault current through the circuit breaker reaches a preset value of 140 A, the I^2t measurement is carried out using the current i_{CB3} . When the I^2t measurement reaches an I^2t calculation or polynomial value (discussed in Section 4), the signal will be sent to trip the circuit breaker

CB3. If the current through the circuit breaker CB3 reaches a very low value compared to the nominal current, then the status of CB3 is updated to 1, meaning that the circuit breaker CB3 has successfully tripped.

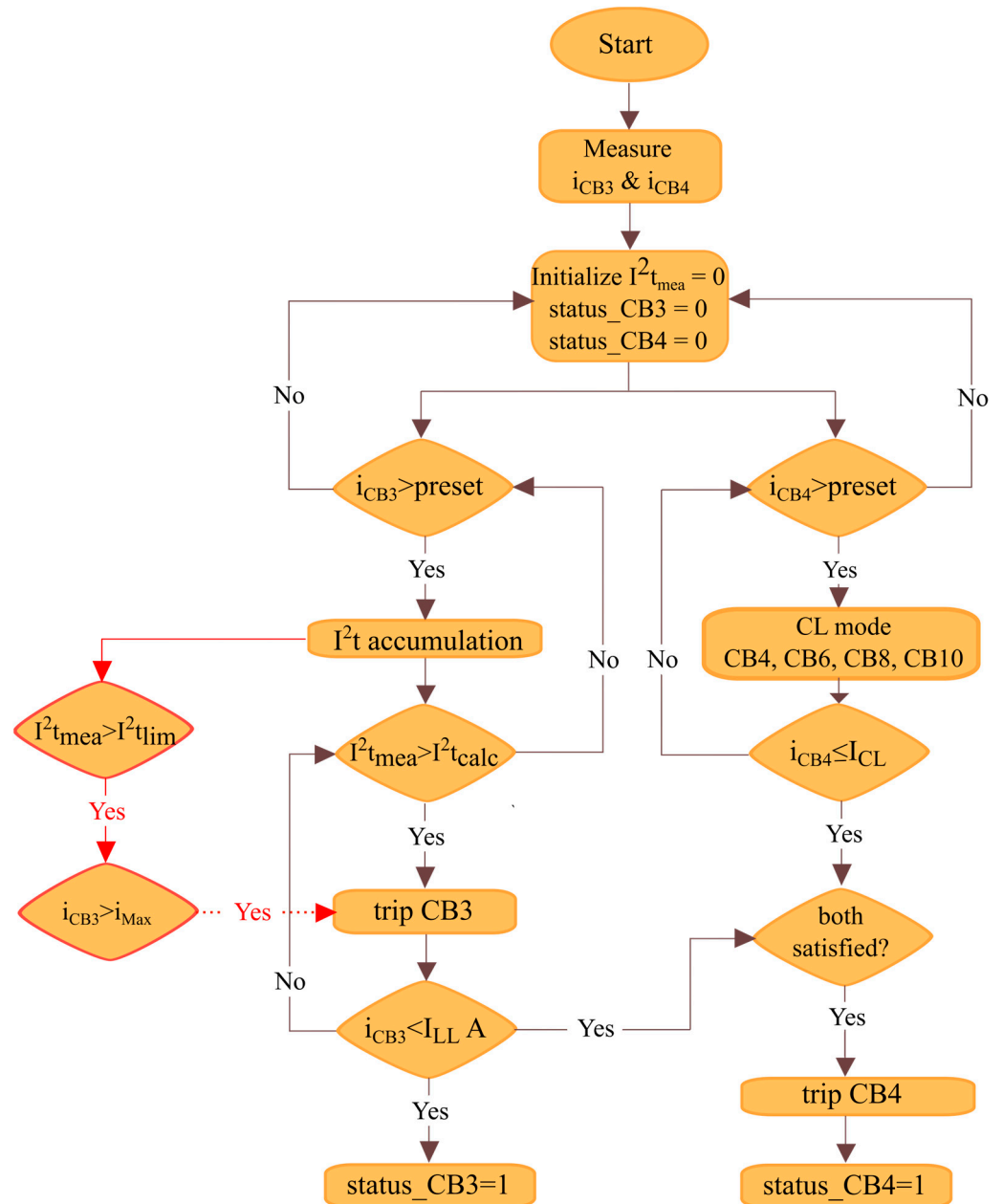


Figure 3. Protection coordination algorithm.

Immediately after the I^2t accumulation, once the I^2t measurement reaches an I^2t limit, the current through circuit breaker CB3 is compared with the maximum value (1200 A) that a circuit breaker can withstand. If the condition is satisfied and the I^2t measurement (I^2t_{mea}) is less than the I^2t polynomial (I^2t_{calc}), the signal is sent to trip the circuit breaker CB1. The I^2t measurement has to be compared with the I^2t limit to make sure that the circuit does not falsely trigger the circuit breaker CB3 for the short duration transients. The I^2t value for a transient which is 8 times the rated current (800 A) for 1 μ s gives a much lower value of 0.64 A^2s . At the same time, the current through the circuit breaker CB4 is measured and then compared with the preset value. Once the current reaches the preset value, a signal is sent to the circuit breakers to operate in current-limiting mode. If the current i_{CB4} is less

than or equal to I_{CL} (current limit value) and the current through CB3 (i_{CB3}) is less than the lower limit (around 10 A), a trip signal is sent to circuit breaker CB4. A simple current limit logic using the TINA TI version V9 software is shown in Figure 3, where a Si MOSFET is considered and then the nominal current of 100 A is allowed to flow through the MOSFET (solid-state circuit breaker). By adjusting the gate voltage from 10 to 3 V, the current value through the MOSFET is limited from 99.6 to 17.5 A, though the load demands 99.6 A, as shown in Figure 4.

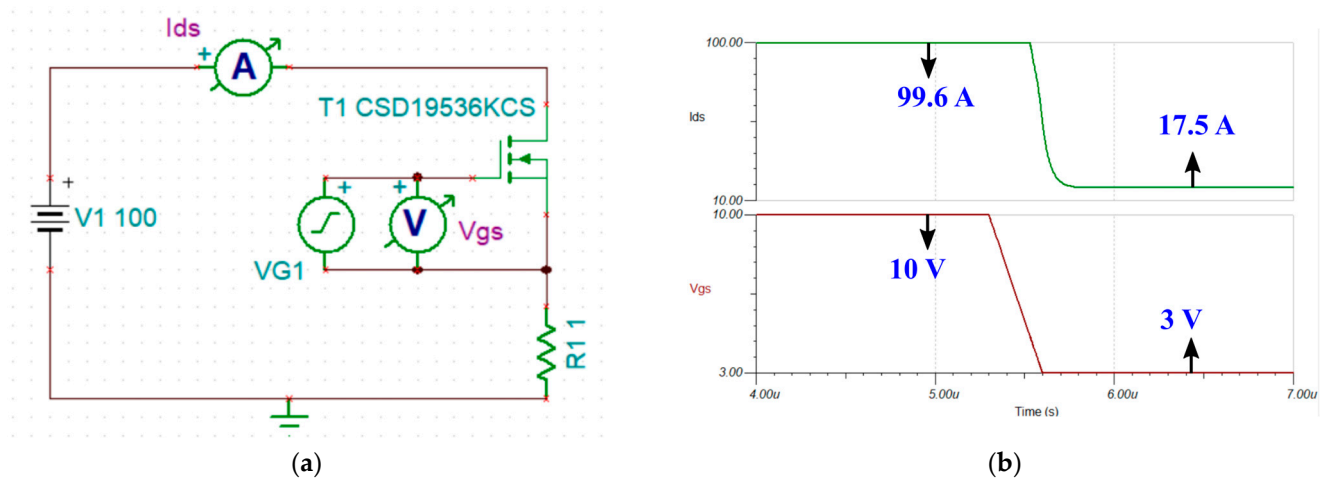


Figure 4. Current-limiting strategy: TINA TI simulation (a) and TINA TI schematic (b) Simulation Results.

Backup Protection

Backup protection is included in the algorithm (shown in Figure 5) to protect the system if any of the circuit breakers in the distribution network fail to operate. When the current flowing through circuit breaker CB3 reaches a maximum value i_{Max} (>1200 A) that a circuit breaker module can handle, a signal will be sent to trip the circuit breaker CB3. If circuit breaker CB3 fails to respond, then the circuit breaker CB1 is tripped immediately, which protects the system from short-circuit fault currents.

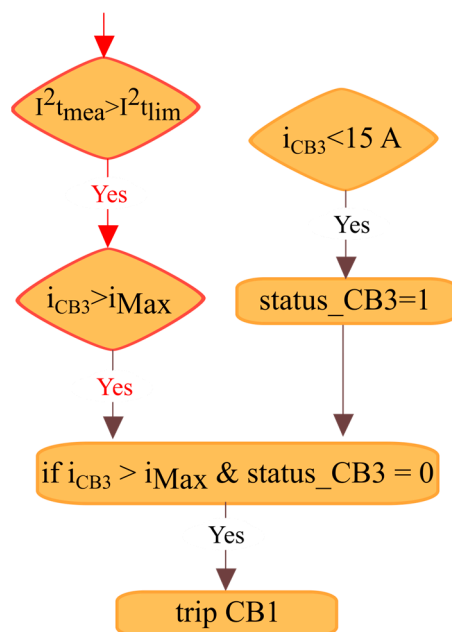


Figure 5. Backup protection.

4. I^2t Curves of the Components in the System

This section presents the I^2t curves for the components of the system, which provide information regarding their thermal capacity. If the component is allowed to continue operating beyond this point, the amount of energy it can handle increases, causing overheating, resulting in component damage. If the I^2t data of all the components in the system is available, the circuit breaker trip time can be adjusted to protect the components in the system from short-circuit faults.

4.1. I^2t of MOSFET

To determine the maximum I^2t of a MOSFET, a pulse test is generally conducted. A pulse is given to the MOSFET, and the rated current is allowed to flow through it \times times. When the junction temperature reaches the maximum limit that a MOSFET can withstand, the MOSFET is turned off. The time taken to reach the maximum temperature is recorded and the corresponding I^2t value is calculated. This process is repeated for $2\times$, $3\times$, $4\times$, \dots $8\times$ times the rated current and the corresponding I^2t values are noted for use in the protection curve.

4.2. I^2t of AC-DC Converter

To observe the rise in temperature for the AC-DC converter at different overload conditions, a MOSFET used in the inverter model is considered. Different overload currents are allowed to flow through it and the temperature variation is noted, which can be seen in Figure 6. The step change in current is given to the MOSFET, which is considered the worst-case scenario and the temperature variations are noted for all the currents. From Figure 6a,b, it can be seen that for $1\times$ and $1.5\times$ rated currents, the steady state device junction temperature is at 74.072 and 109.997 $^{\circ}\text{C}$, respectively, which is under the safe temperature limit of 175 $^{\circ}\text{C}$. From the results, it can be concluded that the MOSFET in the inverter can withstand $1\times$ and $1.5\times$ times the rated current for infinite time. For $2\times$ times the rated current, the steady state temperature is at 159.601 $^{\circ}\text{C}$ and can withstand $2\times$ times the rated current for infinite time, which is shown in Figure 6c. For $5\times$ times the rated current, the temperature is increasing from 74.5 $^{\circ}\text{C}$ to temperatures higher than the 175 $^{\circ}\text{C}$ temperature limit of the MOSFET. To reach the 175 $^{\circ}\text{C}$ limit, it takes approximately 0.881 s, and thus, it can be assumed that the MOSFET can withstand $5\times$ times the rated current for 0.881 s. For $8\times$ times the rated current, the time the temperature takes to reach the limit of 175 $^{\circ}\text{C}$ is 0.287 s. Using the data above, the value of I^2t at different overload conditions is calculated and shown in Table 2.

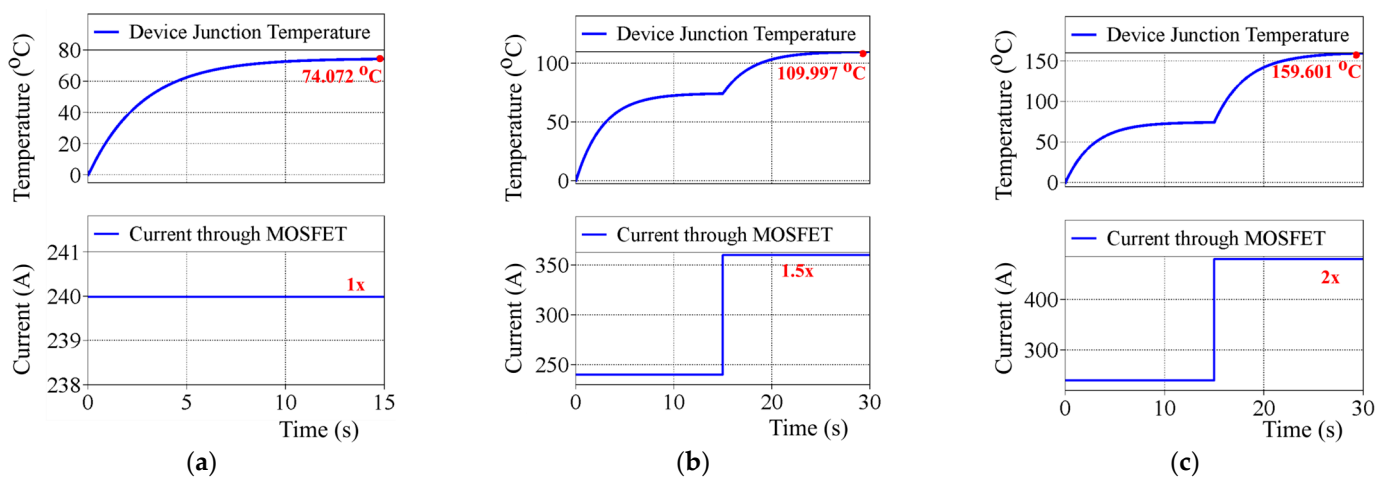


Figure 6. Cont.

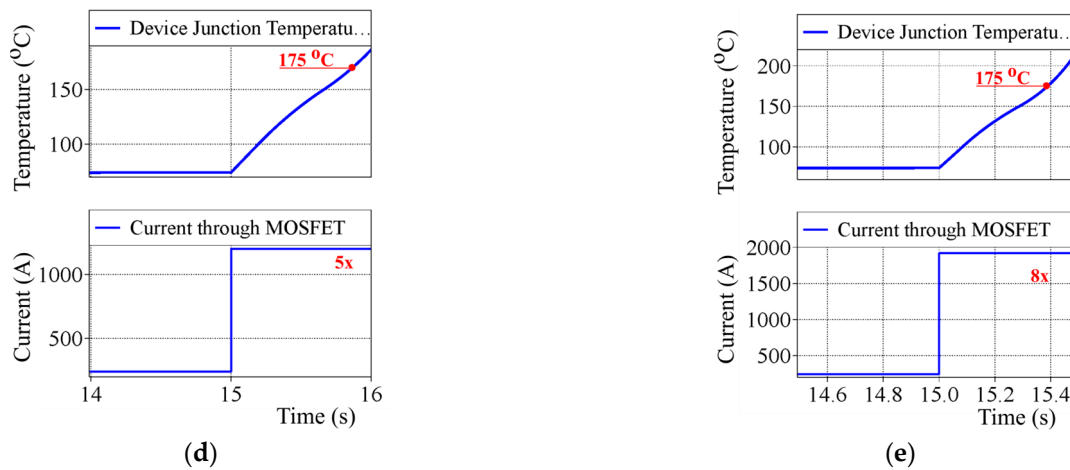


Figure 6. Device junction temperature versus time under different overload conditions: (a) 1× rated current, (b) 1.5× rated current, (c) 2× rated current, (d) 5× rated current, and (e) 8× rated current.

Table 2. I²t values for different overload conditions.

Overload Current	Steady State Temperature (°C)	Time Taken Reach Temperature Limit of MOSFET (Seconds)	I ² t Value
1× (240 A rms)	74.072	Infinite	Infinite
1.5×	109.997	Infinite	Infinite
2×	159.601	Infinite	Infinite
3×	>175	2.711	1,405,382.4
4×	>175	1.435	1,322,496
5×	>175	0.881	1,268,640
6×	>175	0.596	1,235,865.6
7×	>175	0.406	1,145,894.4
8×	>175	0.287	1,057,336.8

4.3. I²t of CABLE

To find the I²t of the cable, the temperature rise in the cable is used, which is given in Equation (1):

$$\frac{d\Delta T}{dt} + \frac{B}{A}\Delta T = \frac{I^2 R}{A} \tag{1}$$

where ΔT —maximum temperature difference in the cable (T_m – T_a);

T_m—Maximum temperature of the cable;

T_a—Ambient temperature;

A—Thermal Capacitance—mass (M)*specific heat (C);

B—Thermal conductance;

I—current through the cable;

R—Resistance of the cable.

By solving the equation, the temperature rise relation is obtained, which is shown in Equation (2).

$$\Delta T = \frac{I^2 R}{B} \left(1 - e^{-\frac{Bt}{A}} \right) \tag{2}$$

From [14,15], considering the worst-case scenario of two motors out of service, each motor has to be rated for 114.3% of the rated power. So, a maximum current of 114.3 A will flow

through the cable in the distribution network. To allow this current, A9XH20KV1050RDC cable is selected for the analysis, which is rated for 279 A at 30 °C. Considering the desired temperature variation of 40 °C and ambient temperature of 50 °C, the resistance of the 10-m cable at maximum operating temperature is given in Equations (3) and (4) below (from the datasheet, DC resistance at 30 °C is 0.387 ohms/km).

$$R_{max} = R_{30} * (1 + \alpha(T - T_{30})) \quad (3)$$

$$= 0.00387 * (1 + 0.00393 * (T_{amb} + \Delta T - 30)) \quad (4)$$

where R_{max} —resistance at the maximum temperature (ambient + desired temperature variation);

R_{30} —Reference resistance of the conductor at 20 °C;

α —Temperature coefficient of resistance (°C⁻¹);

T —Conductor temperature in °C;

ΔT —Desired temperature variation (maximum allowed variation);

T_{30} —Reference temperature (30 °C);

T_{amb} —Ambient temperature (50 °C).

From the above equation, R_{max} is approximately 4.78 milliohms. For the cable selected, the nominal weight is given as 1000 kg/km, and for 10 m, the weight is 10 kg. The thermal time constant using the thermal capacitance and thermal resistance with the assumption that the cable is composed of 25% XLPE and 75% copper by mass is 76.152 min. From Equations (2) and (3), $A = 8307.5$ and $B = 1.81$. By allowing the rated current and 10 times the rated current ($I_{dc} = 114.3$ A) through the cable for a 1 s, the temperature variation is noted as 34.53 and 3453.309 °C, respectively, which are shown in Equations (5) and (6).

$$\Delta T_{rated} = \frac{I_{dc}^2 * R}{B} = 34.53 \text{ °C} \quad (5)$$

$$\Delta T_{10\times} = \frac{(10 * I_{dc})^2 * R}{B} = 3453.309 \text{ °C} \quad (6)$$

With regard to the steady-state temperatures of the selected cable for a continuous current of 114.3 A (worst-case scenario), the maximum temperature of the cable is 84.63 °C (ambient + temperature variation), which is under the maximum permissible temperature and hence the selected cable can be used. Table 3 shows the time taken by the cable to reach the maximum temperature when current multiples (rated current multiples) are allowed to flow through it. Moreover, the plots using the equations are shown in Figure 7, where Figure 7a shows the relation between current and time, and Figure 7b shows the relation between current square and time.

Table 3. Current multiplier vs. time to reach maximum temperature (cable).

Current Multiplier	RMS Current (A)	Time Taken to Reach the Max Temperature
1×	114.3	Infinite
2×	228.63	Infinite
3×	342.9	10.27 s
4×	457.2	6.87 s
5×	571.5	4.05 s
6×	685.8	2.83 s
7×	800.1	1.91 s
8×	914.4	1.6 s

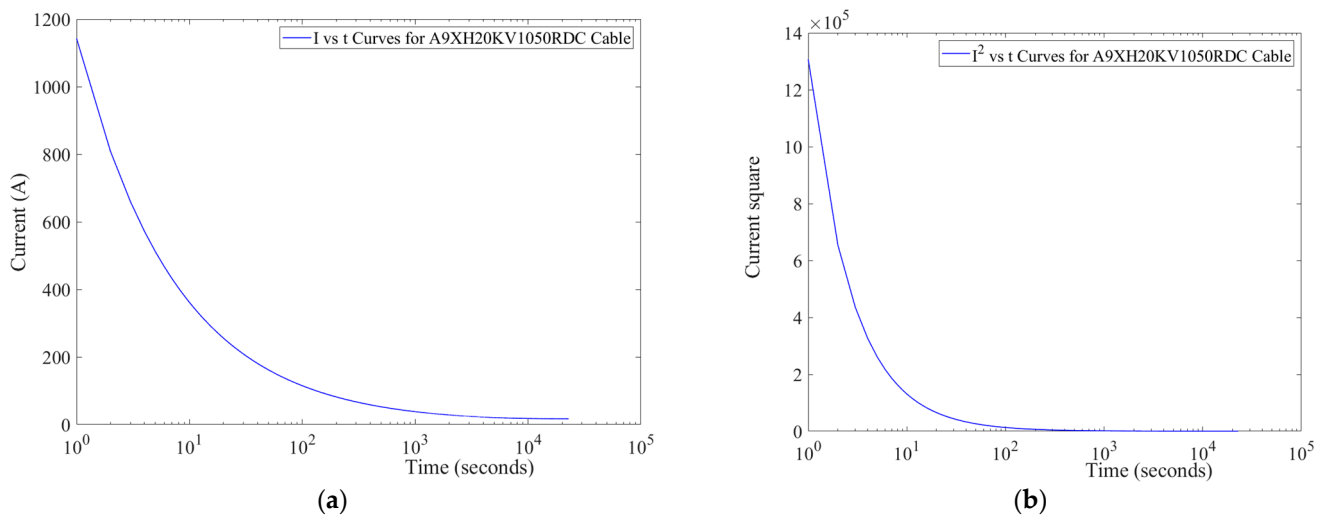


Figure 7. Curves related to A9XH20KV1050RDC cable: (a) I vs. t curve and (b) I² vs. t curve.

4.4. I²t of DC Link Capacitor

To get the I²t of the capacitor, the temperature rise equation is used, which is given in Equation (7):

$$\Delta T = I_{rms}^2 * \frac{esr}{\beta * S} \quad (7)$$

where

ΔT —Temperature change inside the capacitor;

I_{rms} —RMS fault current through the capacitor;

esr —Equivalent series resistance of the capacitor;

β —Heat transfer coefficient;

S —Surface area of the capacitor bank;

m —Mass of the capacitor bank;

C —Specific heat of the material used in the capacitor (polypropylene);

τ —Time constant ($\beta * S * C * m$).

The value of the capacitor at the input of the DC-AC converter is 300 μ F (split bus—+/- 5 kV). Three C44UVGT6450M53K (esr —2.1 milliohms, diameter—116 mm and height—273 mm). Capacitors are rated for 1800 V, and 450 μ F capacitors are connected in series; this combination is connected in parallel to form the 300 μ F, 5000 V capacitance. The temperature variation of 30 °C is considered above the ambient temperature of 50/55 °C, which is the maximum allowable temperature of the capacitor. On solving Equation (7), the value of I_{rms}^2 is 102,797.619 A² (heat transfer coefficient of 25 W/m²K). The calculated value of I²t for one second is 102,797.619 A²s and by using this value, the time required by the capacitor when the multiples of rated current flowing through it is shown in Table 4.

Figure 8 shows the trip curve of all the components that are necessary to understand the protection coordination strategy. To protect the system from short-circuit faults, the circuit breaker has to trip so that the components present in the system are protected. The CB requirement curve shown is considered based on the curves of all the components in the system to protect them from the short-circuit fault current. The maximum time that the components can withstand and the corresponding circuit breaker requirement are shown in Table 5.

Table 4. Current multiplier vs. time to reach maximum temperature (capacitor).

Current Multiplier	RMS Current (A)	Time Taken to Reach the Max Temperature
1×	83.2	Infinite
2×	166.4	Infinite
3×	249.6	1.65
4×	332.8	0.928
5×	416	0.594
6×	499.2	0.412
7×	582.4	0.303
8×	665.6	0.232

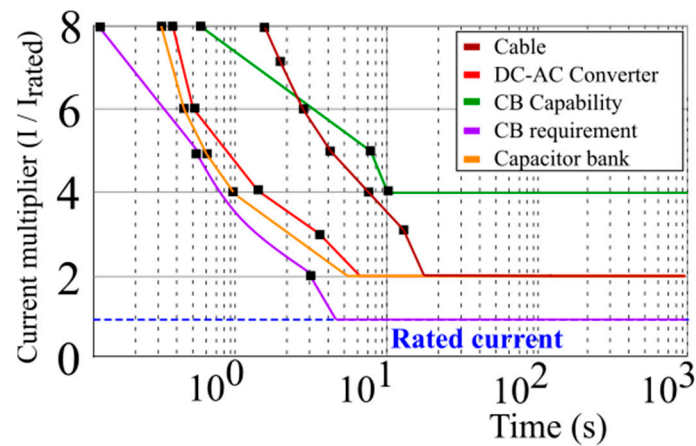


Figure 8. Current multiplier vs. time (trip curve).

Table 5. Current multiplier vs. component trip time.

Component \ Current Multiplier	2×	4×	5×	8×
Cable	Infinite	6.87 s	4.05 s	1.6 s
Capacitor bank	Infinite	928 ms	594 ms	232 ms
Circuit breaker capability	Infinite	Infinite	7.5 s	425 ms
DC-AC converter	Infinite	1.435 s	881 ms	287 ms
Circuit breaker requirement	2 s (DO-160)	NA	500 ms (DO-160)	3 ms (DO-160)

Using the circuit breaker requirement, the curve fitting technique is used to find the best-fit polynomial for the data shown in the table. The polynomial fit is generated using the MATLAB R2023b software, which is shown in Equation (8), and the polynomial fit for the considered circuit breaker requirement data is shown in Figure 9.

$$-51.56x^4 - 159.4x^3 + 1251x^2 + 2.292 \times 10^4x + 3.125 \times 10^4 \tag{8}$$

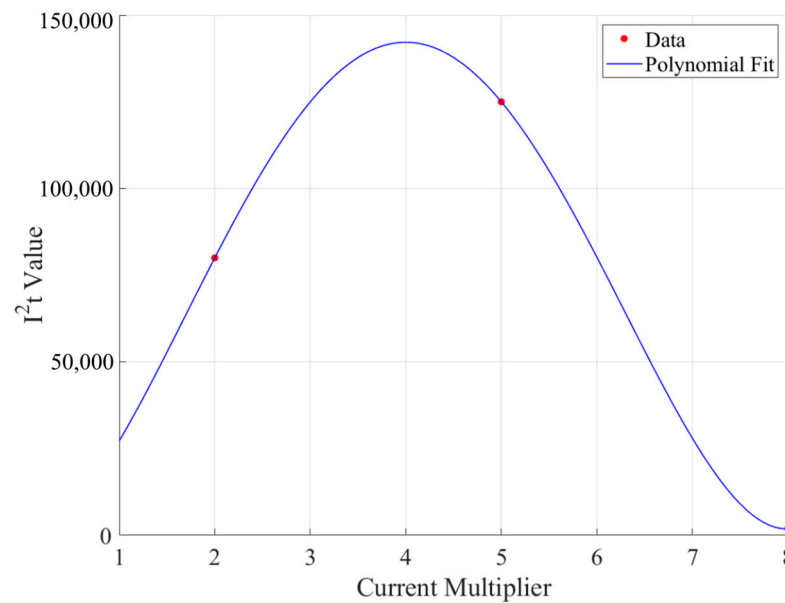


Figure 9. Circuit breaker requirement data and its polynomial fit curve.

5. Results

The proposed protection coordination algorithm is verified using PLECS 4.7.5 simulation software. In this simulation, only one channel out of four is simulated. A short-circuit fault is created between circuit breakers CB3 and CB4. When the short-circuit fault current reaches a preset value of 140 A, the I^2t (measured) algorithm starts accumulation, and at the same time, the I^2t polynomial fit calculation starts. When the I^2t measurement and the I^2t polynomial fit match or the I^2t measurement exceeds the I^2t polynomial fit, the signal will be sent to trip the circuit breaker CB3. Immediately after the short-circuit fault, if the fault current through the circuit breaker CB4 is positive and reaches a preset value, the current limiting algorithm activates and sends the current-limiting signal to the circuit breakers CB4, CB6, CB8, and CB10, which limits the current through these circuit breakers.

Figure 10a,b show the short-circuit fault current through the circuit breaker CB3 and the signal that is sent to the circuit breaker CB3, respectively. A short-circuit fault is created between circuit breakers CB3 and CB4 at 0.11 s, then the fault current starts increasing from the nominal current of 100 A. When the fault current reaches a preset value of 140 A (@0.110001 s), the I^2t measurement gets started (current sensor delay included), which is shown in Figure 11a. The rate of change of the fault current is high in the system due to the low impedance path provided by the cables, so the I^2t measurement has reached a value equal to the I^2t polynomial calculation very quickly, and the signal is sent to trip the circuit breaker CB3, which is shown in Figure 10b. At the same time, once the fault current through the circuit breaker CB4 (i_{CB4}) reaches a preset value of +60 A, a current-limiting signal is sent to the circuit breakers CB4, CB6, CB8, and CB10, which then after the current sensor delay, limits the short-circuit fault current to 20 A, as shown in Figure 12. Due to the current limiting action of circuit breakers CB6, CB8, and CB10, the fault current magnitude of CB3 reduces, which can be seen in Figure 10a. Due to the rapid rise in current, the I^2t measurement (Figure 11a) has reached a value of $2.5 \text{ A}^2\text{s}$, which is equal to the I^2t polynomial value (Figure 11b) at $t = 1.100083 \times 10^{-1} \text{ s}$. As I^2t measurement and I^2t polynomial are equal, a signal is sent to circuit breaker CB3 to trip. Now, both the conditions current through CB3 (i_{CB3}) less than the I_{LL} and current through CB4 (i_{CB4}) is equal to I_{CL} are satisfied, leading to operation of circuit breaker CB4. After successfully tripping the circuit breaker CB3, the signal is sent to trip the circuit breaker CB4, which was in current-limit mode. The current-limiting signal is now removed from the circuit breakers CB6, CB8, and CB10 and continues to provide power to the motor drive, which can be seen in Figure 13.

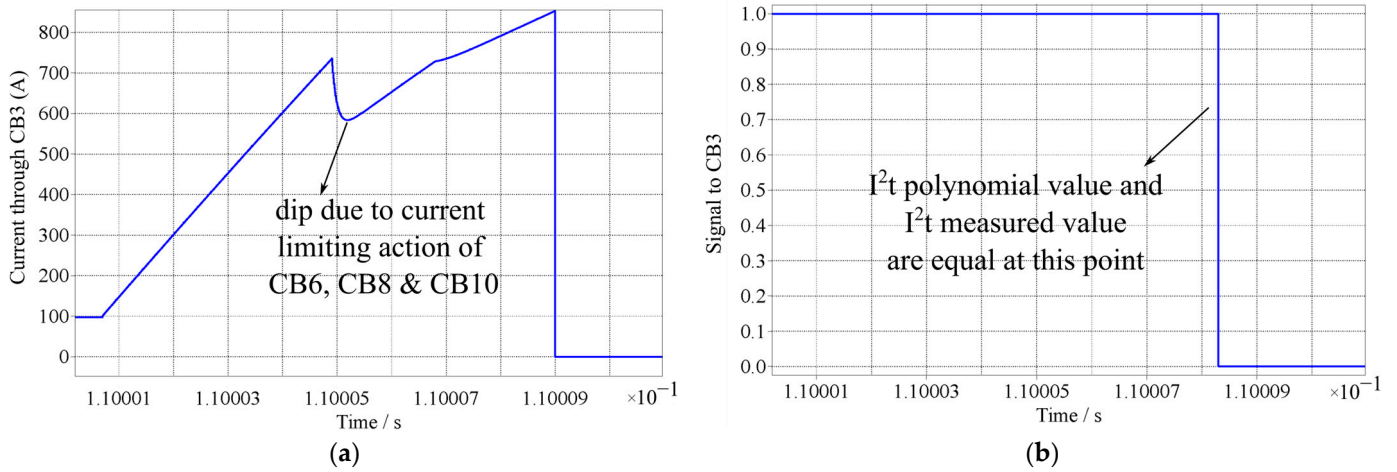


Figure 10. (a) Current through circuit breaker CB3 and (b) signal sent to the circuit breaker.

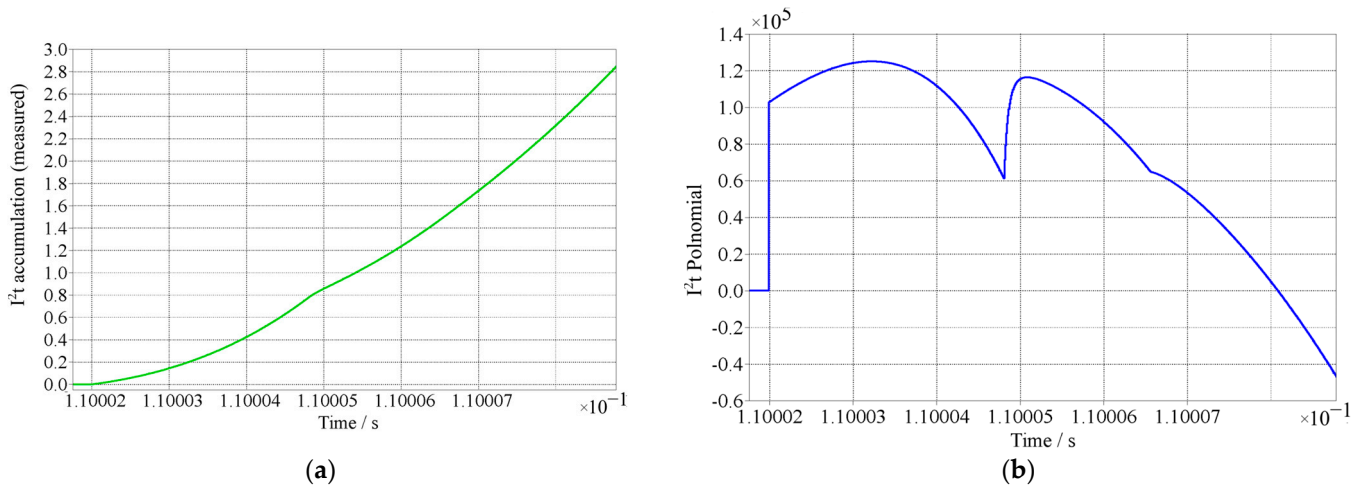


Figure 11. (a) I^2t accumulation (measurement) using the current measurement and (b) I^2t of the polynomial.

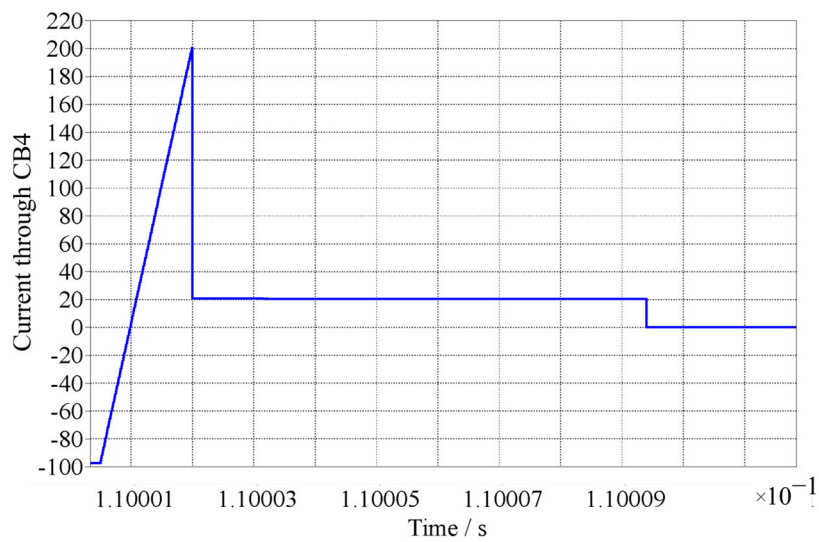


Figure 12. Current through circuit breaker (current limit mode).

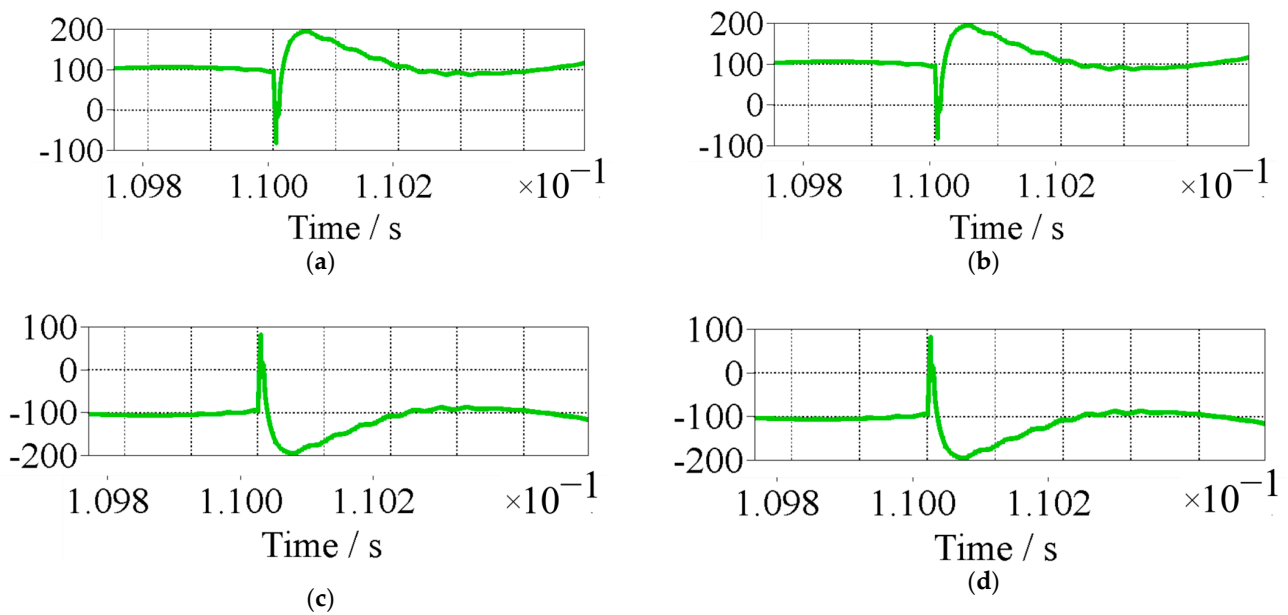


Figure 13. Currents through the circuit breakers: (a) through CB5, (b) through CB7, (c) through CB6, and (d) through CB8.

After clearing the fault, the current through circuit breakers CB5, CB6, CB7, CB8, CB9 and CB10 will return to the nominal current of 100 A. In Figure 13, the current through the circuit breakers CB5, CB6, CB7, and CB8 are shown where the currents through circuit breakers CB5 and CB7 (Figure 13a,b) are exactly opposite to the currents flowing through CB6 and CB8 (Figure 13c,d), respectively, as the capacitors at the input of DC-AC converters are short-circuited through the fault in distribution network 1. Current through CB5 and CB7 or CB6 and CB8 looks similar due to the equal cable inductances and resistances of the cables considered in the system.

5.1. Backup Protection

To validate the backup protection, the signal to the circuit breaker CB3 is maintained high even after the short-circuit fault. When the fault current through the circuit breaker reaches a maximum module capable current of 1200 A (i_{Max}), a trip signal is directly sent to trigger the circuit breaker CB4 irrespective of the I^2t measurement of the circuit to protect the system from fault current, which is shown in Figure 14. This transmission network carries a current of 400 A (four motor drives are connected to it), and as soon as the fault current reaches i_{Max} (1200 A), a trip signal is sent to CB1. During the short-circuit fault, all capacitors at the motor drive input are short circuited, resulting in no power supply to the motors.

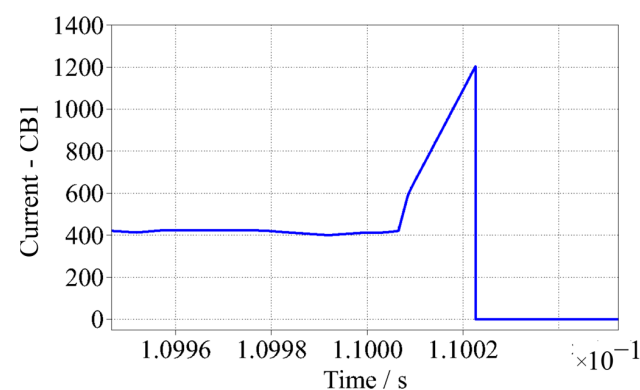


Figure 14. Backup protection—current through CB1.

5.2. Overload Protection

The I^2t algorithm is further demonstrated by overloading the motor by 5 times, causing the distribution cable to be overloaded by 5 times its rated current. As per the circuit breaker specifications, the circuit breaker can withstand 500 amps (5 times the rated current) for 500 milliseconds, so the I^2t value for the circuit breaker is 125,000 A^2s . Figure 15 illustrates the results when a change in load is given at $t = 0.12$ s. Once the current reaches a preset value of 140 A, I^2t measurement accumulates as shown in Figure 15b. For a current of approximately 500 A, the value of the I^2t polynomial is 125,000 A^2s , which can be seen in Figure 15c. From Figure 15b, it can also be seen that I^2t measurement took approximately 500 ms to reach 125,000 A^2s , which is desired as per the circuit breaker requirements. When the I^2t measurement approaches a value near the I^2t polynomial, a signal is sent to trip the circuit breaker CB3, which is shown in Figure 15d and then finally the current through CB3 reaches zero.

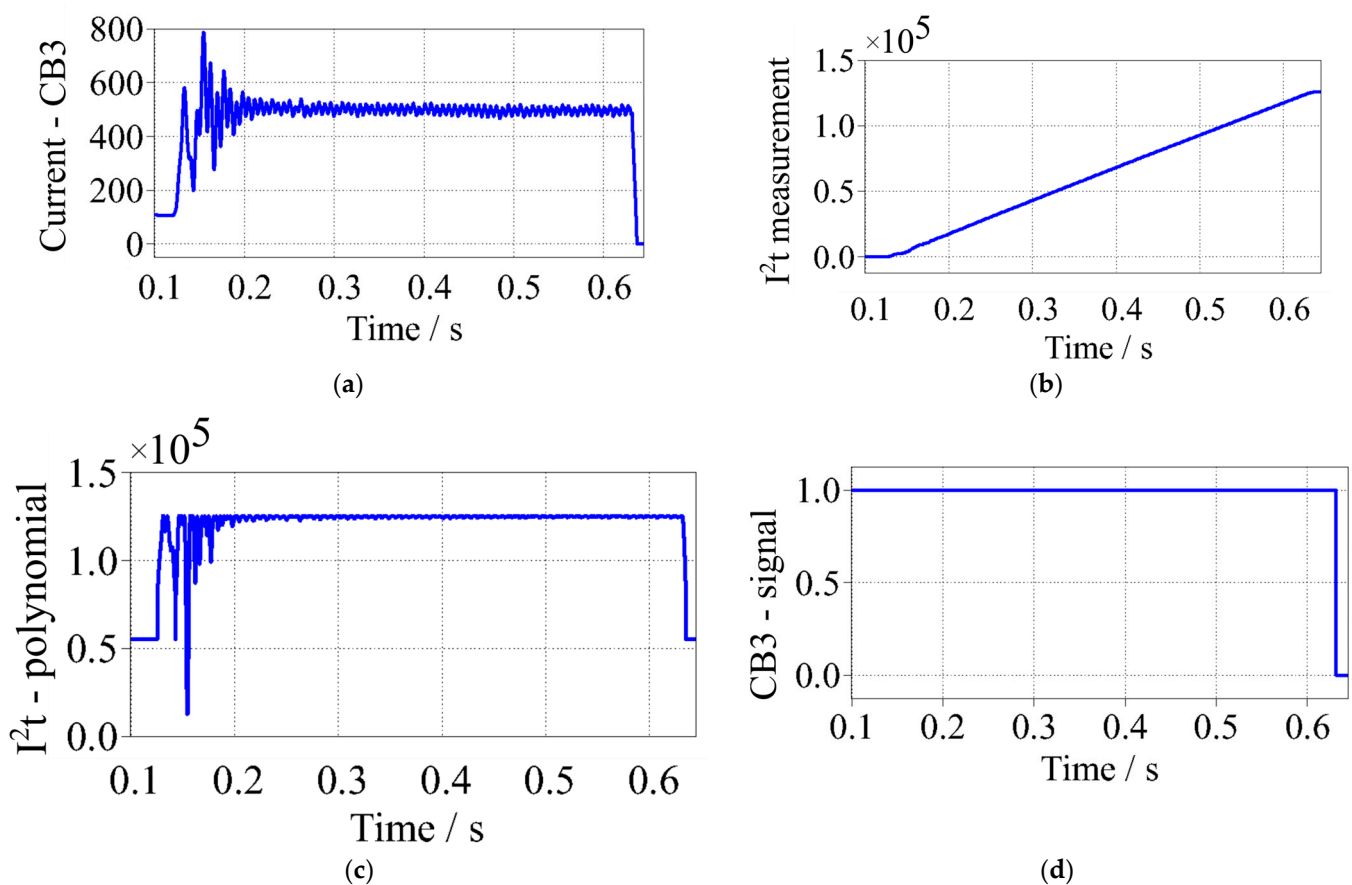


Figure 15. Overload protection: (a) overload current through CB3 (500 A), (b) I^2t accumulation after reaching preset, (c) I^2t polynomial, and (d) signal to circuit breaker CB3.

6. Conclusions

This paper proposes a protection coordination strategy for the distributed electric aircraft propulsion system. To protect the system from short-circuit faults, it employs an I^2t -based protection strategy and current-limiting strategy by operating the circuit breakers closest to the fault. It is by utilizing the current-limit mode on the circuit breakers CB6, CB8, and CB10 that the fault current magnitude through the circuit breaker CB3 is reduced, which contributes to the slowing down of I^2t measurement and provides some time for the I^2t algorithm to send the trip signal to trigger the CB3 when the measured I^2t is greater than I^2t polynomial fit without overheating the components. In the results presented, it is shown that the I^2t algorithm protected the system from the short-circuit fault currents and the current-limiting algorithm helped to reduce the magnitude of fault current generated by

the capacitors at the input of each DC-AC converter. Additionally, an overload current of approximately 5 times the rated current is sent to the circuit breaker, and the I^2t protection took approximately 500 ms, as per the desired circuit breaker requirement to protect the system from short-circuit fault current. The proposed protection coordination strategy can be used in complex architectures by properly choosing the circuit breakers that have to operate in I^2t mode and the circuit breakers that have to be in the current-limit mode. This method requires the I^2t curves of all the components in the system, and by adjusting the curve, the system can be protected from the fault currents without any damage to the components.

Author Contributions: Conceptualization, A.K.R.S., K.R., H.H. and F.W.; methodology, A.K.R.S.; software, A.K.R.S.; validation, A.K.R.S.; formal analysis, A.K.R.S.; investigation, A.K.R.S.; resources, K.R.; data curation, A.K.R.S.; writing—original draft preparation, A.K.R.S.; writing—review and editing, A.K.R.S., K.R., H.H. and F.W.; visualization, A.K.R.S.; supervision, K.R., H.H. and F.W.; All authors have read and agreed to the published version of the manuscript.

Funding: Part of the funding was provided by ARPA-e, Department of Energy, USA.

Data Availability Statement: No new data were created or analyzed in this study. Data sharing is not applicable to this article.

Acknowledgments: The authors would like to thank ARPA-e, Department of Energy, USA under the Award No. DE-AR0001467 for supporting.

Conflicts of Interest: The authors declare no conflicts of interest.

References

- Tom, L.; Khowja, M.; Vakil, G.; Gerada, C. Commercial Aircraft Electrification—Current State and Future Scope. *Energies* **2021**, *14*, 8381. [CrossRef]
- Rajashekara, K. More Electric Aircraft Trends [Technology Leaders]. *IEEE Electrif. Mag.* **2014**, *2*, 4–39. [CrossRef]
- Huang, H.; Challenges in More Electric Aircraft (MEA). IEEE Transportation Electrification Council. 2015. Available online: <https://tec.ieee.org/newsletter/july-august-2015/challenges-in-more-electric-aircraft-mea> (accessed on 23 December 2023).
- Eviation’s Alice Achieves Milestone with First Flight of All-Electric Aircraft. Eviation’s Alice Achieves Milestone with First Flight of All-Electric Aircraft. Available online: www.eviation.com/Press%20Release/eviations-alice-achieves-milestone-with-first-flight-of-all-electric-aircraft/ (accessed on 27 September 2022).
- Fard, M.T.; He, J.; Huang, H.; Cao, Y. Aircraft Distributed Electric Propulsion Technologies—A Review. *IEEE Trans. Transp. Electrif.* **2022**, *8*, 4067–4090. [CrossRef]
- X-57 Maxwell; NASA: Washington, DC, USA. 2023. Available online: <https://www.nasa.gov/aeronautics/x-57-maxwell/> (accessed on 26 July 2023).
- Armstrong, M.J.; Blackwelder, M.; Bollman, A.; Ross, C.; Campbell, A.; Jones, C.; Norman, P. *Architecture, Voltage, and Components for a Turboelectric Distributed Propulsion Electric Grid*; NASA/CR2015-218440; NASA: Washington, DC, USA, 2015.
- Felder, J.L.; Tong, M.T.; Chu, J. Sensitivity of Mission Energy Consumption to Turboelectric Distributed Propulsion Design Assumptions on the N3-X Hybrid Wing Body Aircraft. In Proceedings of the 48th AIAA/ASME/SAE/ASEE Joint Propulsion Conference & Exhibit, Atlanta, GA, USA, 30 July–1 August 2012.
- Berton, J.J.; Haller, W.J. A Noise and Emissions Assessment of the N3-X Transport. In Proceedings of the 52th Aerospace Sciences Meeting, National Harbor, MD, USA, 13–17 January 2014.
- Armstrong, M.J.; Ross, C.A.H.; Blackwelder, M.J.; Rajashekara, K. Trade Studies for NASA N3-X Turboelectric Distributed Propulsion System Electrical Power System Architecture. *SAE Int. J. Aerosp.* **2012**, *5*, 325–336. [CrossRef]
- Siddavatam, A.K.R.; Rajashekara, K.; Huang, H.; Wang, F. A Review of Distributed Electric Aircraft Propulsion Architecture Progression. In Proceedings of the AIAA Aviation 2023 Forum, San Diego, CA, USA, 12–16 June 2023. [CrossRef]
- Gemin, P.; Kupiszewski, T.; Radun, A.; Pan, Y.; Lai, R.; Zhang, D.; Wang, R.; Wu, X.; Jiang, Y.; Galioto, S.; et al. *Architecture Voltage and Components for a Turboelectric Distributed Propulsion Electric Grid (AVC-TeDP)*; NASA CR-2015-218713; NASA: Washington, DC, USA, 2015.
- Ross, C.A.H.; Armstrong, M.; Blackwelder, M.J.; Jones, C.E.; Norman, P.J.; Fletcher, S.D.A. Turboelectric distributed propulsion protection system design trades. In Proceedings of the SAE 2014 Aerospace Systems and Technology Conference, Cincinnati, OH, USA, 23–25 September 2014.

14. Siddavatam, A.K.R.; RajaShekara, K.; Reddy, R.P.; Huang, H.; Krishnamoorthy, H.S.; Dong, Z.; Wang, F. Fault-Tolerant Architectures with Enhanced Bus Protection for Electric/Hybrid Aircraft Systems. *IEEE Trans. Transp. Electrif.* **2023**, *9*, 3564–3578. [[CrossRef](#)]
15. Siddavatam, A.K.R.; Rajashekara, K.; Reddy, R.P.; Huang, H.; Krishnamoorthy, H.S.; Wang, F. A H-type architecture for electric/hybrid-electric aircraft propulsion systems. *IET Electr. Syst. Transp.* **2023**, *13*, e12065. [[CrossRef](#)]

Disclaimer/Publisher's Note: The statements, opinions and data contained in all publications are solely those of the individual author(s) and contributor(s) and not of MDPI and/or the editor(s). MDPI and/or the editor(s) disclaim responsibility for any injury to people or property resulting from any ideas, methods, instructions or products referred to in the content.